Pressure-induced phase transition in MnCO3and its implications on the deep carbon cycle

Eglantine Boulard, Alexander F. Goncharov, Marc Blanchard, Wendy L. Mao

AGU PUBLICATIONS

JGR

Journal of Geophysical Research: Solid Earth

RESEARCH ARTICLE
10.1002/2015JB011901

Key Points:
- We present high-pressure infrared spectroscopy and DFT calculations on $MnCO_3$
- $MnCO_3$ adopts a metastable high-pressure (HP) structure of calcite above 35 GPa
- Metastable HP structures of calcite may represent carbon host in deep Earth

Supporting Information:
- Figure S1

Correspondence to:
E. Boulard,
eglantine.boulard@neel.cnrs.fr

Citation:
Boulard, E., A. F. Goncharov, M. Blanchard, and W. L. Mao (2015), Pressure-induced phase transition in $MnCO_3$ and its implications on the deep carbon cycle, *J. Geophys. Res. Solid Earth*, *120*, 4069–4079, doi:10.1002/2015JB011901.

Received 20 JAN 2015
Accepted 8 MAY 2015
Accepted article online 12 MAY 2015
Published online 8 JUN 2015

Pressure-induced phase transition in $MnCO_3$ and its implications on the deep carbon cycle

Eglantine Boulard[1,2], Alexander F. Goncharov[3], Marc Blanchard[4], and Wendy L. Mao[1,5]

[1]Geological and Environmental Sciences, Stanford University, Stanford, California, USA, [2]Now at Institut NEEL, CNRS, Grenoble, France, [3]Geophysical Laboratory, Carnegie Institution of Washington, Washington, DC, USA, [4]Institut de Minéralogie, de Physique des Matériaux et de Cosmochimie, Sorbonne Universités-UPMC Université Paris 6, UMR CNRS 7590, Muséum National d'Histoire Naturelle, IRD UMR 206, Paris, France, [5]Photon Science, SLAC National Accelerator Laboratory, Menlo Park, California, USA

Abstract The high-pressure behavior of manganese-rich carbonate, rhodochrosite, has been characterized up to 62 GPa by synchrotron-based midinfrared spectroscopy and X-ray diffraction. Modifications in both the infrared spectra and the X-ray diffraction patterns were observed above ~35 GPa, indicating the presence of a high-pressure phase transition at these pressures. We found that rhodochrosite adopts a structure close to $CaCO_3$-VI with a triclinic unit cell ($a = 2.87$ Å, $b = 4.83$ Å, $c = 5.49$ Å, $\alpha = 99.86°$, $\beta = 94.95°$, and $\gamma = 90.95°$ at 62 GPa). Using first-principles calculations based on density functional theory, we confirmed these observations and assigned modes in the new infrared signature of the high-pressure phase. These results suggest that high-pressure metastable phase of calcite may play an important role in carbon storage and transport in the deep Earth.

1. Introduction

The fate of subducted carbonates has profound implications for the global carbon cycle as they represent the major carbon-bearing phases that are recycled into our planet's interior. It is commonly considered that the lower mantle may be too reduced to host carbonates [*McCammon*, 2005; *Frost and McCammon*, 2008; *Rohrbach and Schmidt*, 2011]. However, locally carbonate-enriched areas, such as subducting slabs, might contribute to preserve oxidized carbon-bearing phases in the deep mantle where oxygen fugacity, as controlled by the local mineral assemblage, can be higher. Knowledge of the high-pressure and high-temperature behavior of carbonates is thus essential for modeling the deep carbon cycle. At the Earth's surface, the major carbonate phases are $CaCO_3$ (calcite), $CaMg(CO_3)_2$ (dolomite), and $MgCO_3$ (magnesite). As a result of reactions between carbonates and silicates such as pyroxenes and bridgmanite, Mg-Fe-bearing carbonates should represent the dominant oxidized carbon-bearing phase in the deep mantle and have been the subject of intense research interest [*Biellmann et al.*, 1993; *Wood et al.*, 1996]. Several high-pressure phases of Ca,Mg,Fe-carbonates have been discovered by experiments and theoretical simulations [*Isshiki et al.*, 2004; *Ono et al.*, 2005; *Oganov et al.*, 2006, 2008; *Ono*, 2007; *Boulard et al.*, 2011, 2012], which show complex, composition-dependent high-pressure behavior.

$MnCO_3$ (rhodochrosite) is one of the major calcite-group carbonates present at the surface of the planet where it is mainly found as a vein filling phase in hydrothermal ore deposits [*Hazen et al.*, 2013]. To date, few high-pressure studies have been conducted on rhodochrosite. The Mn^{2+} radius (0.83 Å) lies between that of Mg^{2+} (0.72 Å) and Ca^{2+} (1 Å), which makes it a candidate for understanding the effect of cation size on the differences in the high-pressure phase behavior between $MgCO_3$ and $CaCO_3$. Rhodochrosite is also useful for studying the effect of the substitution of alkaline-earth cations by a *3d* transition metal on the carbonate stability.

At ambient conditions rhodochrosite crystallizes in the calcite structure, which has rhombohedral symmetry (R-3c space group). The unit cell consists of alternating of layers of cations (Mn^{2+}) in sixfold oxygen coordination and trigonal planar $(CO_3)^{2-}$ groups. The high-pressure behavior of $MnCO_3$ is still under debate. A previous study showed that at room temperature, rhombohedral $MnCO_3$ is stable up to 50 GPa [*Santillán and Williams*, 2004]. At high temperature (2273 K), dissociation of $MnCO_3$ into $Mn_3O_4 + 3C + 5/2\ O_2$ was observed at 6–8 GPa [*Liu et al.*, 2001]. Another study reported a phase transition into an orthorhombic phase at 50 GPa −1500 K [*Ono*, 2007].

In a more recent study, a series of transitions under compression at room temperature were observed around 15 and 50 GPa [*Farfan et al.*, 2013]; however, the new structures could not be determined. Here we combine new in situ synchrotron midinfrared (IR) spectroscopy and X-ray diffraction (XRD) measurements collected at high pressure and room temperature with first-principles calculations to resolve the high-pressure behavior of $MnCO_3$ up to 62 GPa.

2. Material and Methods

2.1. Starting Material

Experiments were conducted on a natural rhodochrosite sample from the Sweet Home Mine, Alma, CO. Although the cation composition is dominated by manganese, it also contains low quantities of iron, magnesium, and calcium, corresponding to a composition of $(Mn_{0.976}\ Fe_{0.012}\ Mg_{0.004}\ Ca_{0.002})CO_3$ [*Farfan et al.*, 2013].

2.2. Infrared Spectroscopy

Midinfrared absorption measurements in the 500–4000 cm^{-1} range were performed using a Bruker Vertex 80/v spectrometer at the side station of the high-pressure IR beamline U2A of the National Synchrotron Light Source. The spectral resolution was 4 cm^{-1}, and the beam size on the sample was about 20×20 μm. A powdered rhodochrosite sample embedded in KBr together with ruby balls was loaded into symmetric diamond anvil cell (DAC). KBr was used as a pressure medium. One run was performed with a sufficiently thin sample in order to obtain a good spectral profile by avoiding saturation of the high-intensity band ν_3 and a second run with a thicker sample in order to increase absorbance and get good data quality of the lower intensity bands. Type IIa diamonds anvils with 400 μm culets and a sample chamber diameter of 130 μm were used for this experiment. Pressures measured before and after IR absorbance data collection, were determined from the shift of ruby fluorescence line [*Dorogokupets and Oganov*, 2007]. IR spectra were collected at room temperature upon compression up to 48.7 GPa and decompression back to ambient pressure with a pressure step of about 3 GPa. A background spectrum collected from an area without any sample was used for normalization.

2.3. X-Ray Diffraction

XRD patterns were collected in situ at high pressure and room temperature at beamline 12.2.2 of the Advanced Light Source (ALS), Lawrence Berkeley National Laboratory. A powdered sample of rhodochrosite was loaded between two layers of NaCl into a symmetric DAC with 300 μm flat diamond culets and 100 μm diameter sample chamber. NaCl was used as both a thermal insulator and a pressure calibrant [*Chall et al.*, 2000; *Fei et al.*, 2007]. The sample was compressed at ambient temperature up to 62 GPa. XRD patterns were collected using a monochromatic incident X-ray beam ($\lambda = 0.4133$ Å). The diffraction images were integrated with the Fit2d software [*Hammersley et al.*, 1996]. The one-dimensional diffraction patterns were then treated with the General Structure Analysis System software package [*Larson and Von Dreele*, 2004] using the LeBail method to identify the different phases and refine their lattice parameters.

2.4. Theoretical Methods

First-principles calculations were carried out on $MnCO_3$ at varying pressures, using the unit cell parameters determined from our XRD refinements: rhodochrosite at 13 GPa (*R-3c*; 10 atoms per rhombohedral unit cell with $a = 5.616$ Å; $\alpha = 49.59°$), the high-pressure phase with the $CaCO_3$-VI structure determined by *Merlini et al.* [2012a] and measured at 40 GPa (P1; 10 atoms per unit cell with $a = 2.96$ Å; $b = 4.92$ Å; $c = 5.59$ Å ; $\alpha = 99.67°$; $\beta = 92.99°$; $\gamma = 91.38°$), at 49 GPa (P1; a = 2.92 Å; b = 4.86 Å; c = 5.53 Å; $\alpha = 100.09°$; $\beta = 92.77°$; $\gamma = 91.64°$) and at 60 GPa (P1; a = 2.87 Å; b = 4.83 Å; c = 5.49 Å; $\alpha = 99.86°$; $\beta = 94.95°$; $\gamma = 90.95°$). Crystal structures were calculated using the PWscf code [*Giannozzi et al.*, 2009; http://www.quantum-espresso.org] using density functional theory (DFT) and the generalized gradient approximation to the exchange-correlation functional, with the Perdew-Burke-Ernzerhof parameterization [*Perdew et al.*, 1996]. The ionic cores were described by ultrasoft pseudopotentials from the Garrity-Bennett-Rabe-Vanderbilt library [*Garrity et al.*, 2014]. The wave functions and the charge density were expanded in plane waves with 60 and 600 Ry cutoffs, respectively, leading to a convergence of the total energy of ~1 mRy/atom. For the electronic integration, the Brillouin zone was sampled according to the Monkhorst-Pack scheme

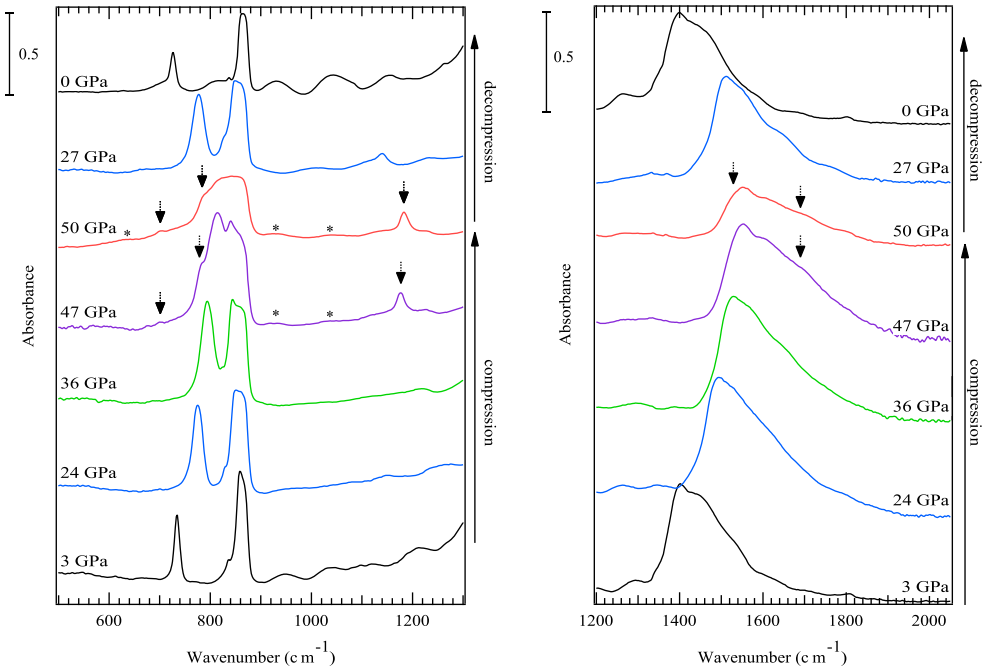

Figure 1. In situ mid-IR spectra as a function of pressure during compression and decompression. The arrows and stars indicate new modes observed at high pressure. The scale bars give the absorbance scale for each panel.

[*Monkhorst and Pack*, 1976], using a shifted $3 \times 3 \times 3$ *k*-point grid. Calculations were spin-polarized and set up to the antiferromagnetic structure with magnetic moments free to relax. Rhodochrosite is known to be antiferromagnetic [*Alikhanov*, 1959]. For the high-pressure phase of $MnCO_3$, other magnetic structures were tested but were found to be less favorable energetically. Atomic positions were relaxed until the residual forces on atoms were less than 10^{-4} Ry/a.u. After relaxation, the magnetic moment on each Mn atom is 4.7 μ_B for all structures investigated. In order to model the IR spectra, the harmonic dynamical matrix and dielectric tensor were calculated at the Brillouin zone center (Γ point), using the linear response theory [*Baroni et al.*, 2001] as implemented in the PHonon code [*Giannozzi et al.*, 2009; http://www.quantum-espresso.org]. A similar approach was previously adopted in order to investigate the IR spectra of the iron oxides hematite and goethite [*Blanchard et al.*, 2008, 2014].

3. Results

3.1. Infrared Measurements

At ambient pressure, the mid-IR spectrum of rhodochrosite displays three main peaks (Figure 1 and Table 1), resulting from fundamental internal vibrations of the C-O bonds in the carbonate radical. (1) A ν_4 band produced by the in-plane bending vibration of the $(CO_3)^{2-}$ group is observed at 726 cm^{-1}, which is in good agreement with previous studies [*Huang and Kerr*, 1960; *Böttcher et al.*, 1992; *Lane and Christensen*, 1997; *Santillán and Williams*, 2004]. (2) A ν_2 mode due to the out-of-plane bending vibration of the $(CO_3)^{2-}$ group is observed at 860 cm^{-1}. Previous studies report the position of this band at ~864 cm^{-1}, which is in

Table 1. Frequency (at 0 GPa) and Pressure Dependence of the Observed IR Vibrational Modes of Rhodochrosite[a]

Frequency (cm^{-1})	Assignment	$d\omega/dP$ (cm^{-1} GPa^{-1})	γ_i	*Santillán and Williams* [2004]
726	ν_4, in plane bend of CO_3^{2-}	$a = 2.13(6)$; $b = 0$	0.32	$d\omega/dP = 1.31$; $\gamma i = 0.20$
860	ν_2 out of plane bend of CO_3^{2-}	$a = -0.32(7)$; $b = 0$	−0.04	$d\omega/dP = -0.03$; $\gamma i = -0.003$
1401	ν_3, asymmetric stretch of CO_3^{2-}	$a = 4.60(35)$; $b = -0.03(1)$	0.36	$d\omega/dP = 2.45$; $\gamma i = 0.19$

[a]Band shifts ($d\omega/dP$) were measured between 0 and 39 GPa ((a and b) the coefficients of the second-order polynomial used following $\omega = \omega_0 + aP + bP^2$). γi: mode Grüneisen parameter defined as: $\gamma_i = K_T/\omega_0(d\omega/dP)_0$, where K_T is the isothermal bulk modulus, ω_0 is the ambient-pressure mode frequency, and $d\omega/dP$ is the mode shift with pressure. We used the bulk modulus determined in this study ($K_0 = 110$ GPa) for calculating the γi.

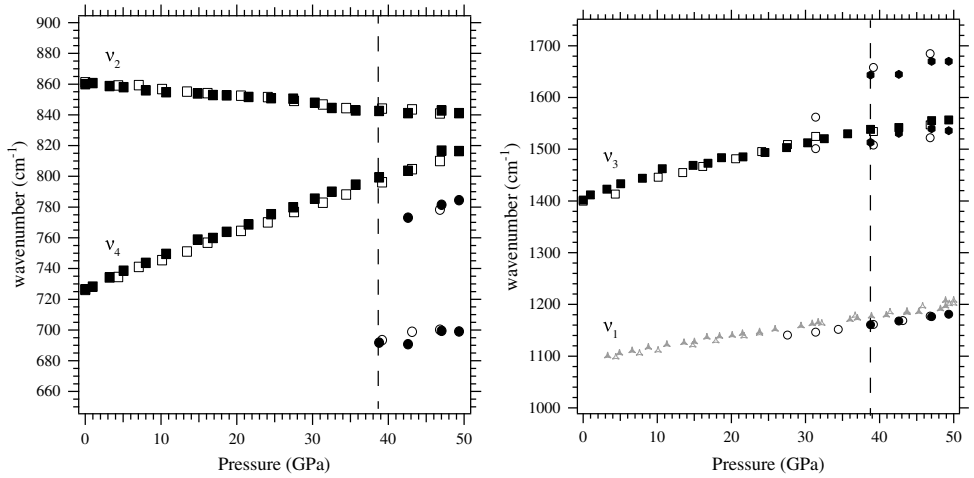

Figure 2. Frequencies of the mid-IR modes as a function of pressure. The new bands are marked by circles. The solid symbols represent the bands observed during compression, and the open symbols represent the ones observed during decompression. For comparison, the position of previously reported Raman v_1 band [*Farfan et al*., 2013] is shown in grey (the solid and open symbols correspond to the data collected upon compression and decompression, respectively). The dashed vertical line corresponds to the pressure of the phase transition (39 GPa).

a good agreement with this work [*Huang and Kerr*, 1960; *Böttcher et al*., 1992; *Lane and Christensen*, 1997; *Santillán and Williams*, 2004]. (3) The strongest band at 1401 cm^{-1} corresponds to the v_3 band associated with the asymmetric stretching vibration of the $(CO_3)^{2-}$ group. This band is slightly lower in frequency than in the previous studies which reported a band at 1433–1450 cm^{-1} [*Huang and Kerr*, 1960; *Santillán and Williams*, 2004]. This may be explained by a compositional effect (the composition reported in *Santillán and Williams* [2004] is of $(Mn_{0.77}Fe_{0.09}Ca_{0.07}Mg_{0.07})CO_3$). In addition, weaker peaks are observed at higher frequencies, which result from the combination of the fundamental modes [*Huang and Kerr*, 1960; *Frost et al*., 2002; *Gunasekaran et al*., 2006]: a band at 1802 cm^{-1} ($v_1 + v_4$), at 2493 cm^{-1} ($v_1 + v_3$), and at 2848 cm^{-1} ($2v_3$). Finally, unexpected satellite of the v_2 band is observed at 837 cm^{-1}. Such additional weak band was previously reported for $CdCO_3$ and $CoCO_3$ by *Weir and Lippincott* [1961] who proposed that these bands stem from the coupling of modes between adjacent $(CO_3)^{2-}$ ions.

No major modification is observed between 0 and 39 GPa (Figure 1). The mid-IR bands were fit with a Lorentzian function in order to extract the band positions, the intensity, and the bandwidths as a function of pressure. Figure 2 shows the evolution of mid-IR band position with pressure. The shifts of these modes were fit with a second-order polynomial, and the results are reported in Table 1; however, the band shifts of v_4 and v_2 were found to be linear ($b = 0$). The two bands v_4 and v_3 shift monotonically to higher frequency with a band shift of 2.13 and 4.38 cm^{-1}/GPa, respectively. The v_2 mode, however, shows a negative shift in frequency with pressure of -0.32 cm^{-1}/GPa. The two lower frequency carbonate bands, v_4 and v_2, merge above 42 GPa becoming unresolvable at 50 GPa. This coincidental degeneracy is not surprising as it has been also reported in other carbonates $FeCO_3$, $MnCO_3$, and $CaCO_3$ [*Kraft et al*., 1991; *Santillán and Williams*, 2004]. This behavior has been interpreted as due to the increase in the coupling of neighboring CO_3 groups, which results in a negative shift of v_2, while an increase in Mn-O strength accounts for a positive shift of v_4 [*Kraft et al*., 1991].

Above 39 GPa, several new IR bands appear at 692, 773, 1161, 1513, and 1643 cm^{-1} (Figures 1 and 2). Additional lower intensity modes are observed at ~620, 931, and 1036 cm^{-1} as marked by stars in Figure 1. The spectral position of the Raman active v_1 after *Farfan et al*. [2013] is also reported on Figure 2. This makes it clear that the new mode at 1161 cm^{-1} stems from the activation of v_1 in IR. Appearance of new modes and decrease of the rhodochrosite modes' amplitudes (by a factor of about 2) suggest a phase transition. The band positions and the pressure shifts of IR bands in the high-pressure phase are reported in Table 2. With the exception of v_4, reductions in the pressure slope are observed above 39 GPa for the rhodochrosite modes that persist in the high-pressure phase pressure range. In contrast to our results,

Table 2. Frequency (at 38 GPa) and Pressure Dependence of the Observed IR Vibrational Modes Associated to the High-pressure Phase[a]

Frequency (cm^{-1})	Assignment	$d\omega/dP$ (cm^{-1} GPa^{-1})
692	HP-phase ν_4, in plane bend of CO_3^{2-}	0.88
773 (41 GPa)	HP-phase ν_4, in plane bend of CO_3^{2-}	1.52
1161	HP-phase ν_1, symmetric stretch of CO_3^{2-}	1.94
1513	HP-phase ν_3, asymmetric stretch of CO_3^{2-}	1.02
1643	HP-phase ν_3, asymmetric stretch of CO_3^{2-}	3.94

[a]Band shifts ($d\omega/dP$) were measured between 39 and 50 GPa with a linear equation.

Santillán and Williams [2004] did not observe any new vibration modes in the IR spectrum of $MnCO_3$ between 0 and 50 GPa. A possible explanation for this discrepancy is that our composite sample was effectively thicker allowing us to observe weak absorption peaks such as the new modes observed above 39 GPa.

The IR spectrum collected at room pressure after decompression is consistent with the spectrum before compression, indicating that the phase transition is reversible. However, upon decompression the new IR band at 1167 cm^{-1} persists until 27 GPa, demonstrating some hysteresis.

3.2. X-Ray Diffraction

XRD patterns were collected upon compression at room temperature from 0 to 62 GPa (Figure 3). The patterns can be indexed with the carbonate rhombohedral cell R-3c between 0 and ~15 GPa. We observed changes in the diffraction pattern starting at 15 GPa, in good agreement with previous observations [*Farfan et al.*, 2013]. While no additional XRD peaks are observed, there is a peculiar evolution of the diffraction peak positions: *d*-spacings for the (110) and (012) diffraction peaks remain constant upon compression, while other diffraction peaks such as the (014) continue to decrease with pressure. A fit of the XRD patterns collected above 15 GPa with a rhombohedral cell also leads to an error greater than 13%. We fit the pressure versus volume data to a second-order Birch-Murnaghan equation of state between 0 and 15 GPa and obtained the following parameters: $K_0 = 110(11)$ GPa and $V_0 = 310(2)$ A^3. This is slightly lower than the bulk modulus reported by *Ono* [2007] (126 GPa), but very close to the one reported by *Zhang and Reeder* [1999] (107 GPa), which can be explained by the pressure range chosen to refine the bulk modulus in the different studies: 0–50 GPa [*Ono*, 2007] and 0–7 GPa [*Zhang and Reeder*, 1999]. Please note that the composition of the rhodochrosite samples used in both of these studies is very close to our starting material. The ambient condition unit cell parameters could be confidently extrapolated from our measurements: $a_0 = 4.77(1)$ Å; $c_0 = 15.68$ (3) Å, which are in good agreement with previous studies [*Zhang and Reeder*, 1999; *Ono*, 2007]. Upon compression, the *c* axis is about 4 times

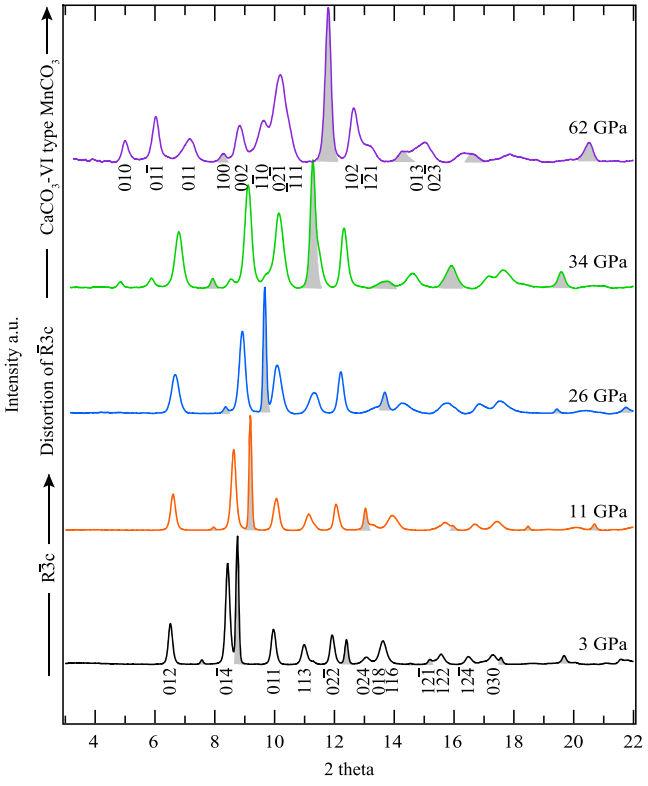

Figure 3. High-pressure XRD patterns ($\lambda = 0.4133$) of $MnCO_3$ collected during compression up to 62 GPa showing three pressure domains corresponding to the rhombohedral phase R-3c from 0 to ~15 GPa, the distorted phase from 15 to 34 GPa, and the high-pressure phase above 34 GPa. Indexing of the peaks for the rhodochrosite and the high-pressure phase is shown on the XRD pattern collected at 3 GPa and 62 GPa, respectively. XRD peaks of the pressure medium NaCl are indicated in grey.

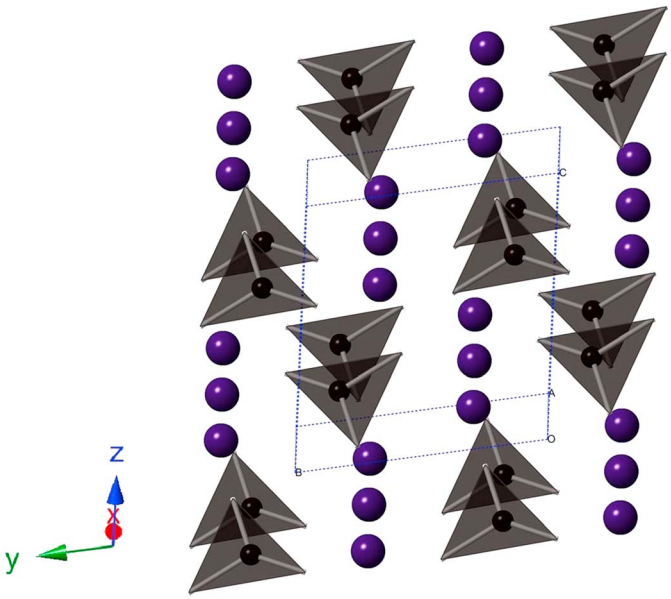

Figure 4. Structure of the high-pressure phase related to the $CaCO_3$-VI phase of calcite [*Merlini et al*., 2012a]. CO_3 groups appear in black, and Mn^{2+} atoms are shown as violet spheres.

more compressible than the *a* axis. This anisotropic compression is typical of rhombohedral carbonates [*Ross*, 1997; *Zhang and Reeder*, 1999; *Lavina et al*., 2010a] and reflects the incompressibility of C-O bonds in the *a-b* plane compared to Mn-O bonds. The CO_3 groups act as incompressible rigid units, while the MnO_6 octahedra show significant compression under pressure.

Above ~34 GPa, we observed dramatic modifications in the diffraction pattern. New diffraction peaks emerged and increased in intensity under further compression indicating a phase transition (Figure 3 and Figure S1 in the supporting information). These changes occur at a similar pressure to the first appearance of the new IR modes described previously. This new phase persists to at least 62 GPa, the highest pressure in our study.

4. Discussion

A recent in situ Raman study reported changes in the Raman modes shifts around 17 and 35 GPa and concluded that these changes are not related to an electronic spin transition of Mn^{2+}, such as it has been observed for Fe^{2+} in $FeCO_3$ at similar pressure, but to a change in the crystal structure [*Farfan et al*., 2013]. However, no structures were proposed. Here our in situ IR and XRD experiments confirm the presence of a structural phase transition near ~35 GPa. *Ono* [2007] reported a phase transition at a slightly higher pressure (50 GPa) after laser heating at ~1500–2000 K and proposed an orthorhombic structure. However, the structure proposed by *Ono* [2007] does not fit the XRD patterns measured of our study. In a recent study on the $(Mn,Ca)CO_3$ solid solution, *Shi et al*. [2012] reported an increasing linear shift in the pressure of the transitions $CaCO_3$-I ⇒ $CaCO_3$-II ⇒ $CaCO_3$-III with Mn content and predicted that these phase transitions would take place at 19 and 26 GPa for end-member $MnCO_3$. However, the phase observed by in situ XRD between 15 and 35 GPa in the present study is not consistent with the $CaCO_3$-II structure [*Merrill and Bassett*, 1975] but may rather be related to a distortion due to nonhydrostatic conditions.

Above 35 GPa, the new XRD patterns do not correspond to $CaCO_3$-II or $CaCO_3$-III but instead are consistent with another calcite high-pressure polymorph: post $CaCO_3$-III [*Catalli and Williams*, 2005]. The structure of this polymorph was recently described by *Merlini et al*. [2012a] from refinement of single crystal XRD results. They proposed a small triclinic unit cell with $Z = 2$ and named the phase $CaCO_3$-VI [*Merlini et al*., 2012a; *Vizgirda and Ahrens*, 1982]. This structure has parallel planar CO_3 groups, but the layers of cations do not alternate with the layers of $(CO_3)^{2-}$ as in the calcite structure [*Merlini et al*., 2012a] (Figure 4). We found that this structure is consistent with the in situ XRD patterns of the high-pressure $MnCO_3$ phase we measured above 35 GPa (Figure 5a). We obtained a unit cell of $V = 74$ Å^3 at 62 GPa (2.87 Å; $b = 4.83$ Å; $c = 5.49$ Å; $\alpha = 99.86°$; $\beta = 94.95°$; $\gamma = 90.95°$). Figure 5b shows the pressure-density data measured on $MnCO_3$ in the present study. From the difference between the density predicted by the equation of state (EOS) of rhodochrosite at 62 GPa and that measured experimentally for the high-pressure phase, we estimated an increase of density of ~2% at ~35 GPa.

In order to interpret the IR spectrum for the high-pressure phase, we carried out first-principles calculations of the IR spectra of $MnCO_3$ below and above the phase transition. Atomic positions were relaxed at constant volume, using the experimental unit cell parameters determined here from XRD refinements. Calculated IR spectra are reported in Figure 6. At 13 GPa, calculations confirm the assignment of the three absorption

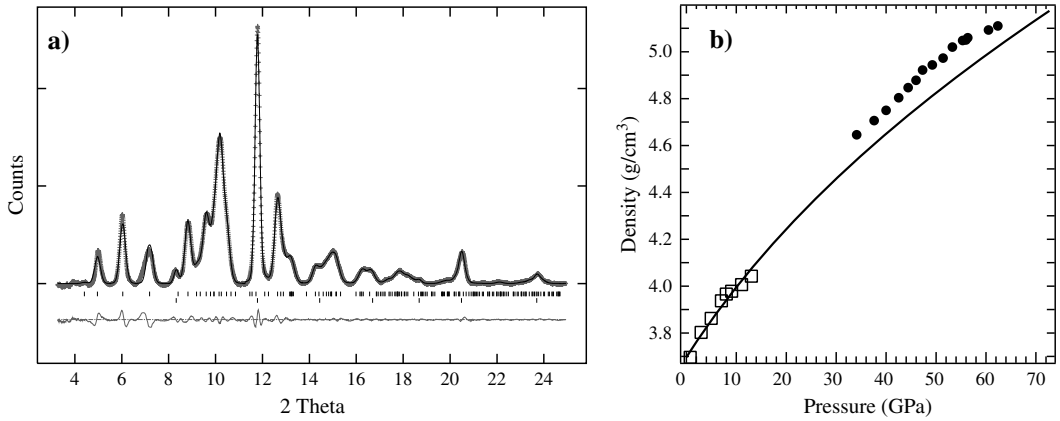

Figure 5. (a) XRD pattern of $MnCO_3$ at 62 GPa and room temperature. Background has been subtracted. The crosses represent observed data after subtraction of the background, and the solid line represents the profile refinement. For this refinement we used an assemblage of a triclinic $CaCO_3$-VI phase [*Merlini et al.*, 2012a] (upper ticks) and the NaCl-B2 phase (lower ticks). Residual between observations and fit is shown below the spectrum. (b) Pressure-density data for rhodochrosite (squares) and the high pressure phase (circles). The line denotes the EOS of rhodochrosite determined with the present data (between 0 and 13 GPa) and extrapolated to high pressures.

bands observed experimentally. The three computed carbonate modes v_4, v_2, and v_3 of rhodochrosite are at 713, 789, and 1478 cm^{-1}, respectively (Table 3). These theoretical frequencies are lower than the experimental ones for the bending modes by ~7%, while the stretching mode is well reproduced (<1%) (Figure 7). While all the C-O bond distances are equal within the $(CO_3)^{2-}$ group in the rhombohedral phase (1.13 Å at 13 GPa), the C-O interatomic distances split into 1.11, 1.22, and 1.39 Å at 55 GPa in the high-pressure phase. As a result, the doubly degenerate E_u modes corresponding to v_4 and v_3 fundamentals split to 2A mode components upon this phase transition. This is observed in our calculations, which show a large splitting of v_4 and v_3 in good agreement with our experimental observations. The A_{2u} (v_2) and A_{1u} (v_1) modes become A modes. This makes previously inactive A_{1u} (v_1) mode active in IR as it becomes A.

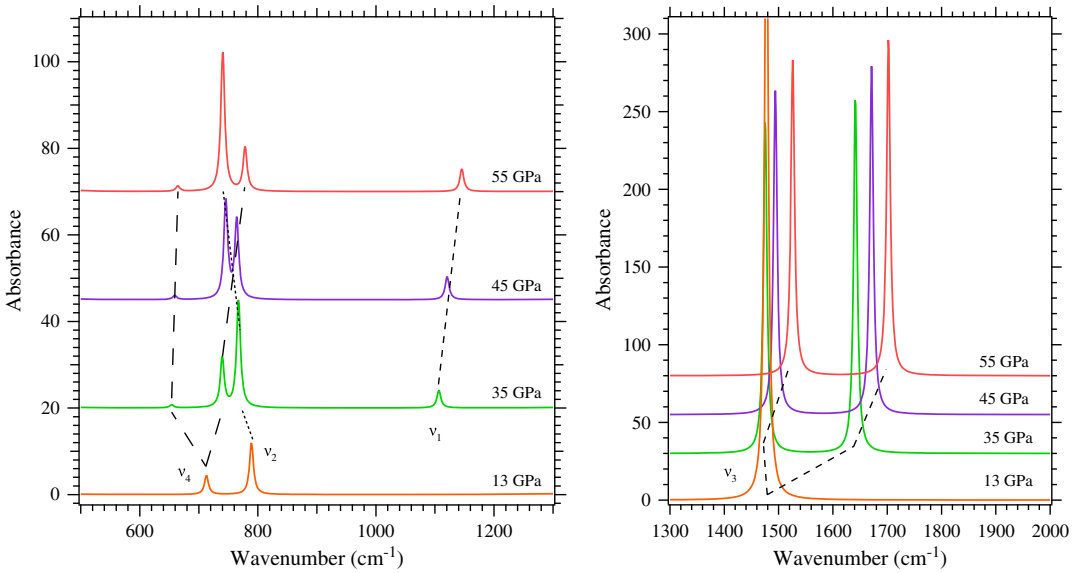

Figure 6. Theoretical IR absorption spectra for rhodochrosite (13 GPa) and the high-pressure $CaCO_3$-VI structure phase. Calculations are conducted for spherical $MnCO_3$ particles inserted in a homogeneous KBr matrix. After the phase transition, v_4 and v_3 split into two modes. The dotted lines are guides for the eye of the wave number evolution of each mode with pressure.

Table 3. Calculated IR Vibrational Modes for the High Pressure $CaCO_3$-VI Phase of $MnCO_3$[a]

	13 GPa	35 GPa	45 GPa	55 GPa	$d\omega/dP$ (cm^{-1} GPa^{-1})
ν_4 (cm^{-1})		654	659	664	0.53
	713	740	764	778	1.93
ν_2 (cm^{-1})	*789*	767	745	741	−1.33
ν_1 (cm^{-1})		1107	1121	1145	1.95
ν_3 (cm^{-1})	*1478*	1475	1494	1526	2.53
		1641	1671	1702	3.05

[a]The bands associated with rhodochrosite are shown in italic (13 GPa). The $d\omega/dP$ of the high-pressure phase modes were calculated between 35 and 55 GPa.

While the calculated frequencies of bending modes are systematically lower than the experimental frequencies, it should be noted that the pressure evolution for all of the vibrational modes is in good agreement with our experimental results. Upon compression, calculations show that the out-of-plane bending vibration of the CO_3 group, ν_2, shows a negative shift to lower wavenumbers, while a positive shift is observed for the in-plane bending vibration ν_4 leading to a crossover at about 45 GPa. Experimental IR spectra were collected only up to the mixing of ν_2 and ν_4, and a complete crossover was not observed. In our experimental IR spectra, the ambient phase rhodochrosite modes coexist with these new modes leading to the presence of multiple modes in the 650–900 cm^{-1} area. The uncertainty stemming from this mixture of phases prevented us from determining the position of the new ν_2. The lower intensity modes (marked by stars in Figure 1) may stem from combination modes of fundamentals (ν_2 and ν_4) and translational modes. The IR spectrum of $CaCO_3$-VI has been previously described by *Catalli and Williams* [2005] for a Ca-bearing carbonate. In a good agreement with our observations, the $CaCO_3$-VI IR spectra show the presence of a splitting of the ν_4 and ν_3 IR modes, plus the IR activation of the ν_1.

With the decomposition of $(Mg,Ca)CO_3$ (dolomite) into $CaCO_3$ and $MgCO_3$ at mantle conditions [*Biellmann et al.*, 1993], it is usually assumed that calcite and magnesite and their respective high-pressure polymorphs are the main oxidized carbon-bearing phases in the Earth's interior. It has been shown experimentally that upon compression, $CaCO_3$ adopts the aragonite structure above ~2 GPa and then transforms to postaragonite above 40 GPa [*Dickens and Bowen*, 1970; *Ono et al.*, 2005]. In fact the different polymorphs $CaCO_3$-II, $CaCO_3$-III, and $CaCO_3$-VI correspond to metastable phases of $CaCO_3$. However, together with a previous study on dolomite [*Merlini et al.*, 2012a], our study shows that $CaCO_3$-VI may play a role in carbon

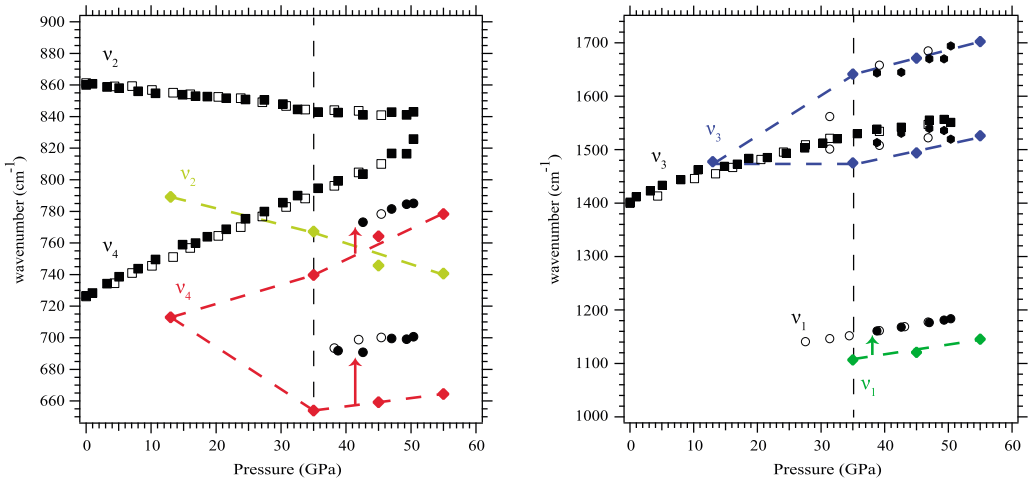

Figure 7. Theoretical and experimental band positions as a function of pressure. The colored symbols represent the theoretical calculations, and the black markers represent the experimental measurements. Red: the frequencies of the modes associated with ν_4, light green: ν_2, dark green: ν_1, and blue: ν_3. The lines between the calculated band positions are guides for the eye. The arrows indicate assignments of the experimental modes. The vertical lines indicate the pressure of the phase transition (~35 GPa).

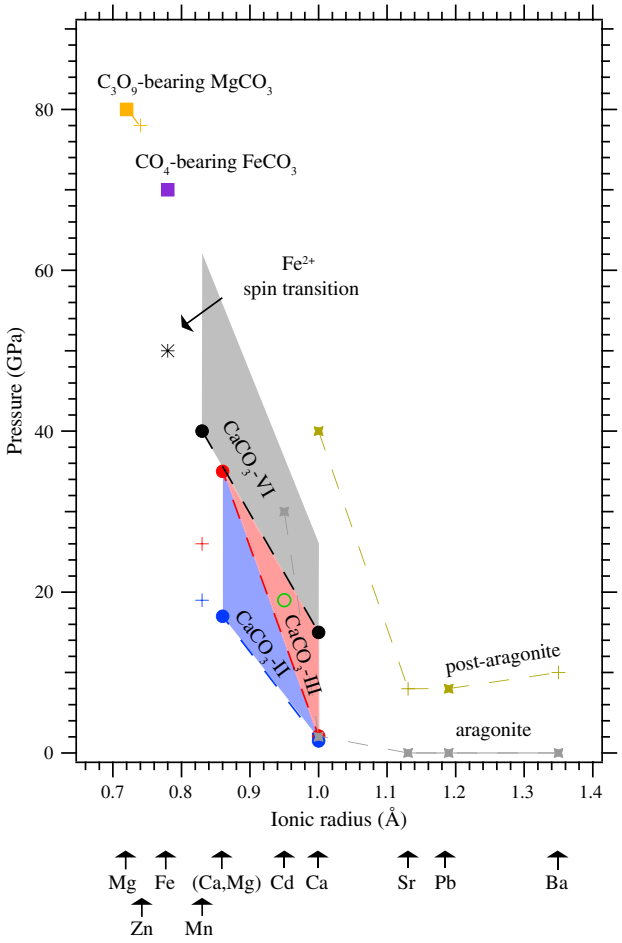

Figure 8. Main phase transition boundaries for divalent carbonates at high pressure as a function of ionic radius. The value of the cation radius for dolomite (Ca,Mg) is an average value for the Ca^{2+} and Mg^{2+} radii. The closed markers represent previously reported experimental points from *Minch et al.* [2009] ($PbCO_3$), *Ono et al.* [2005] and *Dickens and Bowen* [1970] ($CaCO_3$), *Merlini et al.* [2012a, 2012b] ($(Ca,Mg)CO_3$ and $CaCO_3$), *Minch et al.* [2010] ($CdCO_3$), the present study ($MnCO_3$), and *Boulard et al.* [2011, 2012] ($FeCO_3$ and $MgCO_3$). The crosses are theoretical points from *Oganov et al.* [2008] ($SrCO_3$, $BaCO_3$) and *Bouibes and Zaoui* [2014] $ZnCO_3$. The pressure of the Fe spin transition in siderite is noted by a star [*Lavina et al.*, 2009, 2010b].

storage and transport in the deep Earth. Due to the high cation coordination site in the aragonite structure, the incorporation of small cations (<1 Å, Ca^{2+}) is limited.

Figure 8 shows a summary of the different phase boundary pressures as a function of ionic radius from experimental and theoretical previous studies. The aragonite structure is indeed observed at ambient conditions for large cation (>1 Å) compositions such as $SrCO_3$, $PbCO_3$, and $BaCO_3$ and at high pressure in $CaCO_3$ and $CdCO_3$ in which cation sizes are intermediate (1 and 0.95 Å, respectively) [*Dickens and Bowen*, 1970; *Liu and Lin*, 1997]. The aragonite structure has not been observed in carbonate systems with smaller cations. Our study shows that it is possible for small cation-bearing carbonates to adopt the metastable $CaCO_3$-VI structure. This observation is not surprising because in this structure the cation site volume is smaller than in aragonite, and therefore, it is more likely to host cations smaller than Ca^{2+} (<1 Å) [*Merlini et al.*, 2012a]. $CaCO_3$-VI is also more dense than aragonite [*Merlini et al.*, 2012a]. In agreement with our observation, the stability of the metastable $CaCO_3$-II and $CaCO_3$-III type structures has been recently reported for the $CaMg_{0.6}Fe_{0.4}(CO_3)_2$ dolomite composition [*Merlini et al.*, 2012b]. Metastable $CaCO_3$ high-pressure structures may represent oxidized carbon hosts at mantle condition for carbonate compositions containing relatively small cations. The smallest cations (Fe^{2+} and Mg^{2+}), however, show a different high-pressure behavior with the stability of calcite structure being maintained up to ~70–80 GPa above, which these compositions adopt a tetrahedrally coordinated carbon structure [*Bouibes and Zaoui*, 2014; *Boulard et al.*, 2012, 2011; *Oganov et al.*, 2008].

5. Conclusion

The high-pressure behavior of $MnCO_3$ has been studied by in situ XRD and IR spectroscopy up to 62 GPa and 50 GPa, respectively. Evidence for structural changes are observed above ~35 GPa, where we found that $MnCO_3$ adopts a $CaCO_3$-VI type triclinic structure. Modeling of the IR spectra based on DFT calculations supports this conclusion. Although additional experiments are needed at the high temperature existing in the Earth's mantle conditions, our study shows that due to its ability to host small cations and its high density and stability at high pressure, the high-pressure $MnCO_3$ in the $CaCO_3$-VI structure may represent a potential oxidized carbon-bearing phase for enabling transport of carbon into the Earth's deep interior.

Acknowledgments
Mid-IR spectroscopy experiments were performed at the U2A beamline at NSLS, which was supported by COMPRES, the Consortium for Materials Properties Research in Earth Sciences under NSF cooperative agreement EAR 11–57758 and the DOE-NNSA (DE-FC03-03 N00144, CDAC). The use of NSLS was supported by the U.S. Department of Energy (DOE), Office of Science, Office of Basic Energy Sciences (BES), under contract DE-AC02-98CH10886. We thank Z. Liu for his assistance with the mid-IR spectroscopy experiments. XRD was performed at the high-pressure beamline 12.2.2, ALS which is supported by the DOE-BES under contract DE-AC02-05CH11231. We thank J. Yan, J. Knight, and A. MacDowell for their assistance with XRD experiments at ALS. We also thank M. Scott for providing the rhodochrosite sample. W.L. Mao is supported by NSF, Geophysics grants EAR-1141929. E. Boulard and A.F. Goncharov acknowledge support from the Deep Carbon Observatory. DFT calculations were performed using HPC resources from GENCI-IDRIS (grant 2014-i2014041519).

References

Alikhanov, R. A. (1959), Neutron diffraction investigation of the antiferromagnetism of the carbonates of manganese and iron, *Sov. Phys. JETP-USSR*, *9*, 1204–1208.

Baroni, S., S. de Gironcoli, A. D. Corso, and P. Giannozzi (2001), Phonons and related crystal properties from density functional perturbation theory, *Rev. Mod. Phys.*, *73*, 515–562.

Biellmann, C., P. Gillet, F. Guyot, J. Peyronneau, and B. Reynard (1993), Experimental evidence for carbonate stability in the Earth's lower mantle, *Earth Planet. Sci. Lett.*, *118*, 31–41, doi:10.1016/0012-821X(93)90157-5.

Blanchard, M., M. Lazzeri, F. Mauri, and E. Balan (2008), First-principles calculation of the infrared spectrum of hematite, *Am. Mineral.*, *93*, 1019–1027.

Blanchard, M., E. Balan, P. Giura, K. Béneut, H. Yi, G. Morin, C. Pinilla, M. Lazzeri, and A. Floris (2014), Infrared spectroscopic properties of goethite: Anharmonic broadening, long-range electrostatic effects and Al substitution, *Phys. Chem. Miner.*, *41*, 289–302.

Böttcher, M. E., P.-L. Gehlken, and E. Usdowski (1992), Infrared spectroscopic investigations of the calcite-rhodochrosite and parts of the calcite-magnesite mineral series, *Contrib. Mineral. Petrol.*, *109*, 304–306.

Bouibes, A., and A. Zaoui (2014), High-pressure polymorphs of $ZnCO_3$: Evolutionary crystal structure prediction, *Sci. Rep.*, *4*, 5172, doi:10.1038/srep05172.

Boulard, E., A. Gloter, A. Corgne, D. Antonangeli, A. Auzende, J.-P. Perrillat, F. Guyot, and G. Fiquet (2011), New host for carbon in the deep Earth, *Proc. Natl. Acad. Sci. U.S.A.*, *108*, 5184–5187, doi:10.1073/pnas.1016934108.

Boulard, E., et al. (2012), Experimental investigation of the stability of Fe-rich carbonates in the lower mantle, *J. Geophys. Res.*, *117*, B02208, doi:10.1029/2011JB008733.

Catalli, K., and Q. Williams (2005), A high-pressure phase transition of calcite-III, *Am. Mineral.*, *90*, 1679–1682, doi:10.2138/am.2005.1954.

Chall, M., B. Winkler, P. Blaha, and K. Schwarz (2000), Structure and properties of NaCl and the Suzuki phase Na_6CdCl_8, *J. Phys. Chem. B*, *104*(6), 1191–1197.

Dickens, B., and S. Bowen (1970), Refinement of the crystal structure of the aragonite phase of $CaCO_3$, *J. Res. Natl. Bur. Stand. A. Phys. Chem.*, *75A*, 27–32.

Dorogokupets, P. I., and A. R. Oganov (2007), Ruby, metals, and MgO as alternative pressure scales: A semiempirical description of shock-wave, ultrasonic, X-ray, and thermochemical data at high temperatures and pressures, *Phys. Rev. B*, *75*, 024115.

Farfan, G. A., E. Boulard, S. Wang, and W. L. Mao (2013), Bonding and electronic changes in rhodochrosite at high pressure, *Am. Mineral.*, *98*, 1817–1823, doi:10.2138/am.2013.4497.

Fei, Y., A. Ricolleau, M. Frank, K. Mibe, G. Shen, and V. Prakapenka (2007), Toward an internally consistent pressure scale, *Proc. Natl. Acad. Sci. U.S.A.*, *104*, 9182–9186, doi:10.1073/pnas.0609013104.

Frost, D., and C. McCammon (2008), The redox state of Earth's mantle, *Annu. Rev. Earth Planet. Sci.*, *36*, 389–420.

Frost, R. L., W. N. Martens, L. Rintoul, E. Mahmutagic, and J. T. Kloprogge (2002), Raman spectroscopic study of azurite and malachite at 298 and 77 K, *J. Raman Spectrosc.*, *33*, 252–259, doi:10.1002/jrs.848.

Garrity, K. F., J. W. Bennett, K. M. Rabe, and D. Vanderbilt (2014), Pseudopotentials for high-throughput DFT calculations, *Comput. Mater. Sci.*, *81*, 446–452.

Giannozzi, P., et al. (2009), QUANTUM ESPRESSO: A modular and open-source software project for quantum simulations of materials, *J. Phys. Condens. Matter*, *21*, 395502, doi:10.1088/0953-8984/21/39/395502.

Gunasekaran, S., G. Anbalagan, and S. Pandi (2006), Raman and infrared spectra of carbonates of calcite structure, *J. Raman Spectrosc.*, *37*, 892–899, doi:10.1002/jrs.1518.

Hammersley, A. P., S. O. Svensson, M. Hanfland, A. N. Fitch, and D. Hausermann (1996), Two-dimensional detector software: From real detector to idealised image or two-theta scan, *High Press. Res.*, *14*, 235–248, doi:10.1080/08957959608201408.

Hazen, R. M., R. T. Downs, A. P. Jones, and L. Kah (2013), Carbon mineralogy and crystal chemistry, *Rev. Mineral. Geochem.*, *75*, 7–46, doi:10.2138/rmg.2013.75.2.

Huang, C. K., and P. F. Kerr (1960), Infrared study of the carbonate minerals, *Am. Mineral.*, *45*, 311–324.

Isshiki, M., T. Irifune, K. Hirose, S. Ono, Y. Ohishi, T. Watanuld, E. Nishibori, M. Takata, and M. Sakata (2004), Stability of magnesite and its high-pressure form in the lowermost mantle, *Nature*, *427*, 60–63, doi:10.1029/2000C000736.

Kraft, S., E. Knittle, and Q. Williams (1991), Carbonate stability in the Earth's mantle: A vibrational spectroscopic study of aragonite and dolomite at high pressures and temperatures, *J. Geophys. Res.*, *96*, 17,997–18,009, doi:10.1029/91JB01749.

Lane, M. D., and P. R. Christensen (1997), Thermal infrared emission spectroscopy of anhydrous carbonates, *J. Geophys. Res.*, *102*, 25,581–25,592, doi:10.1029/97JE02046.

Larson, A. C., and R. B. Von Dreele (2004), General Structure Analysis System (GSAS) Los Alamos Natl. Lab. Rep. LAUR, pp. 86–748.

Lavina, B., P. Dera, R. T. Downs, V. Prakapenka, M. Rivers, S. Sutton, and M. Nicol (2009), Siderite at lower mantle conditions and the effects of the pressure-induced spin-pairing transition, *Geophys. Res. Lett.*, *36*, L23306, doi:10.1029/2009GL039652.

Lavina, B., P. Dera, R. Downs, W. Yang, S. Sinogeikin, Y. Meng, G. Shen, and D. Schiferl (2010a), Structure of siderite $FeCO_3$ to 56 GPa and hysteresis of its spin-pairing transition, *Phys. Rev. B*, *82*, 1–7, doi:10.1103/PhysRevB.82.064110.

Lavina, B., P. Dera, R. T. Downs, O. Tschauner, W. Yang, O. Shebanova, and G. Shen (2010b), Effect of dilution on the spin pairing transition in rhombohedral carbonates, *High Press. Res.*, *30*, 224–229, doi:10.1080/08957959.2010.485391.

Liu, L., and C. Lin (1997), A calcite → aragonite-type phase transition in $CdCO_3$, *Am. Mineral.*, *82*, 643–646.

Liu, L., C. Lin, and Y. Yang (2001), Formation of diamond by decarbonation of $MnCO_3$, *Solid State Commun.*, *118*, 195–198.

Mccammon, C. (2005), The paradox of mantle redox, *Science*, *308*, 807–808.

Merlini, M., M. Hanfland, and W. A. Crichton (2012a), $CaCO_3$-III and $CaCO_3$-VI, high-pressure polymorphs of calcite: Possible host structures for carbon in the Earth's mantle, *Earth Planet. Sci. Lett.*, *333–334*, 265–271, doi:10.1016/j.epsl.2012.04.036.

Merlini, M., W. A. Crichton, M. Hanfland, M. Gemmi, H. Müller, I. Kupenko, and L. Dubrovinsky (2012b), Structures of dolomite at ultrahigh pressure and their influence on the deep carbon cycle, *Proc. Natl. Acad. Sci. U.S.A.*, *109*, 13,509–14, doi:10.1073/pnas.1201336109.

Merrill, B. L., and W. A. Bassett (1975), The crystal structure of $CaCO_3$ (II), a high-pressure metastable phase of calcium carbonate, *Acta Crystallogr.*, *B31*, 343–349.

Minch, R., L. Dubrovinsky, A. Kurnosov, L. Ehm, K. Knorr, and W. Depmeier (2009), Raman spectroscopic study of $PbCO_3$ at high pressures and temperatures, *Phys. Chem. Miner.*, *37*, 45–56, doi:10.1007/s00269-009-0308-0.

Minch, R., et al. (2010), High-pressure behavior of otavite ($CdCO_3$), *J. Alloys Compd.*, *508*, 251–257, doi:10.1016/j.jallcom.2010.08.090.

Monkhorst, H. J., and J. D. Pack (1976), Special points for Brillouin-zone integrations, *Phys Rev B*, *13*, 5188–5192.

Oganov, A. R., C. W. Glass, and S. Ono (2006), High-pressure phases of $CaCO_3$: Crystal structure prediction and experiment, *Earth Planet. Sci. Lett.*, *241*, 95–103, doi:10.1016/j.epsl.2005.10.014.

Oganov, A. R., S. Ono, Y. Ma, C. W. Glass, and A. Garcia (2008), Novel high-pressure structures of $MgCO_3$, $CaCO_3$ and CO_2 and their role in Earth's lower mantle, *Earth Planet. Sci. Lett.*, *273*, 38–47, doi:10.1016/j.epsl.2008.06.005.

Ono, S. (2007), High-pressure phase transformation in $MnCO_3$: A synchrotron XRD study, *Mineral. Mag.*, *71*, 105–111, doi:10.1180/minmag.2007.071.1.105.

Ono, S., T. Kikegawa, Y. Ohishi, and J. Tsuchiya (2005), Post-aragonite phase transformation in $CaCO_3$ at 40 GPa, *Am. Mineral.*, *90*, 667–671, doi:10.2138/am.2005.1610.

Perdew, J. P., K. Burke, and M. Ernzerhof (1996), Generalized gradient approximation made simple, *Phys. Rev. Lett.*, *77*, 3685–3868.

Rohrbach, A., and M. W. Schmidt (2011), Redox freezing and melting in the Earth's deep mantle resulting from carbon-iron redox coupling, *Nature*, *472*(7342), 209–12.

Ross, N. L. (1997), The equation of state and high-pressure behavior of magnesite, *Am. Mineral.*, *82*, 682–688.

Santillán, J., and Q. Williams (2004), A high-pressure infrared and X-ray study of $FeCO_3$ and $MnCO_3$: Comparison with $CaMg(CO_3)_2$-dolomite, *Phys. Earth Planet. Inter.*, *143–144*, 291–304, doi:10.1016/j.pepi.2003.06.007.

Shi, W., M. E. Fleet, and S. Shieh (2012), High-pressure phase transitions in Ca-Mn carbonates (Ca, Mn) CO_3 studied by Raman spectroscopy, *Am. Mineral.*, *97*, 999–1001.

Vizgirda, J., and T. J. Ahrens (1982), Shock compression of aragonite and implications for the equation of state of carbonates, *J. Geophys. Res.*, *87*, 4747–4758, doi:10.1029/JB087iB06p04747.

Weir, C. E., and E. R. Lippincott (1961), Infrared studies of aragonite, calcite, and vaterite type structures in the borates, carbonates, and nitrates, *J. Res. Nat. Bur. Stand. A. Phys. Chem.*, *65*(3), 173–183.

Wood, B. J., A. Pawley, and D. R. Frost (1996), Water and carbon in the Earth's mantle, *Philos. Trans. R. Soc. London*, *354*, 1495–1511.

Zhang, J., and R. J. Reeder (1999), Comparative compressibilities of calcite-structure carbonates: Deviations from empirical relations, *Am. Mineral.*, *84*, 861–870.